Very Low-Noise Differential Radiometer at 30 GHz for the PLANCK LFI

Beatriz Aja, *Student Member, IEEE*, Eduardo Artal, *Member, IEEE*, Luisa de la Fuente, *Member, IEEE*, Juan Pablo Pascual, *Member, IEEE*, Angel Mediavilla, Neil Roddis, Danielle Kettle, W. Frank Winder, Lluis Pradell i Cara, and Pedro de Paco

***Abstract*—The PLANCK mission of the European Space Agency is devoted to produce sky maps of the cosmic microwave background radiation. The low-frequency instrument is a wide-band cryogenic microwave radiometer array operating at 30, 44, and 70 GHz. The design, test techniques, and performance of the complete differential radiometer at 30 GHz are presented. This elegant breadboard 30-GHz radiometer is composed of a front-end module (FEM) assembled at the Jodrell Bank Observatory, Cheshire, U.K., and a back-end module assembled at the Universidad de Cantabria, Cantabria, Spain, and Telecomunicació, Universitat Politécnica de Catalunya, Barcelona, Spain. The system noise temperature was excellent, mainly due to the very low noise performance of the FEM amplifiers, which achieved an average noise temperature of 9.4 K.**

***Index Terms*—Cosmic microwave background (CMB), cryogenic, low-noise amplifier (LNA), microwave radiometer, PLANCK low-frequency instrument (LFI).**

I. Introduction

PLANCK is the third-generation space cosmic microwave background (CMB) temperature anisotropy mission, following the cosmic microwave background explorer (COBE) and Wilkinson microwave anisotropy probe (WMAP). PLANCK will provide wide-frequency coverage with two instruments, i.e., the bolometer-based high-frequency instrument (HFI) and the radiometer-based low-frequency instrument (LFI), having outstanding angular resolution and sensitivity [1]. The LFI contains 22 differential radiometers covering three frequency bands with ultralow-noise amplifiers based on cryogenic indium phosphide (InP) high electron-mobility transistors (HEMTs). There are four radiometers at 30 GHz, six at 44 GHz, and 12 at 70 GHz [2], [3], all of them with a 20% effective bandwidth. Fig. 1 shows a schematic of an LFI radiometer chain, which comprises two receivers.

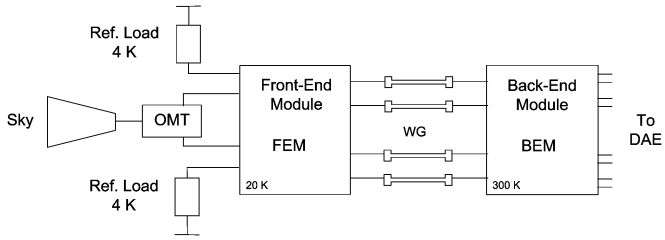

Fig. 1. Schematic of an LFI radiometer.

A feed horn [4], an orthomode transducer (OMT), a front-end module (FEM), and a back-end module (BEM) constitute an LFI radiometer.

The feed horn is in the focal plane and the OMT separates the incoming radiation into two perpendicular linearly polarized components that propagate independently through the two parallel branches. High performance of these passive components has crucial importance in high-sensitivity CMB experiments.

The two main units, i.e., the FEM and BEM, are connected via 1-m-long waveguides. The FEM contains the most sensitive part of the receiver, where pseudocorrelation is implemented. It operates at 20 K to lower the system noise and to have better sensitivity. This temperature is provided by a closed-cycle hydrogen sorption cryocooler [5], which will be capable of proving 1.2 W of cooling power at 20 K. This stringent requirement on low power consumption caused the decision to split the radiometer into a cold FEM and a warm BEM at 300 K. The BEM provides further amplification, defines the band, and detects the signal.

Section II describes the overall architecture and operating principles of the radiometer. Sections III and IV give details of the design and performance characterization of the FEM and BEM. Section V deals with the overall performance characterization of the radiometer. Finally, conclusions are drawn in Section VI.

II. Radiometer Architecture

A. Overview

The LFI receivers are coherent direct detection radiometers. The detected voltage results from the noise power without using intermediate frequencies. High sensitivity is due to low-noise temperatures and wide bandwidths of the amplifiers. On the

Manuscript received September 30, 2004; revised December 17, 2004 and January 12, 2005. This work was supported by the Physic Particles and Radioastronomy Committee, U.K., and by the Spanish Ministerio de Ciencia y Tecnología under Space National Program ESP2002-04141-C03-02/03.

B. Aja, E. Artal, L. de la Fuente, J. P. Pascual, and A. Mediavilla are with the Departamento de Ingeniería de Comunicaciones, Universidad de Cantabria, Escuela Técnica Superior de Ingenieros de Telecomunicación, 39005 Santander, Spain (e-mail: beatriz@ dicom.unican.es).

N. Roddis, D. Kettle, and W. F. Winder are with the Jodrell Bank Observatory, The University of Manchester, Cheshire SK11 9DL, U.K. (e-mail: nr@jb.man.ac.uk).

L. Pradell i Cara is with the Departamento de Teoría del Senyal i Comunicacions, Escola Técnica Superior d'Enginyeria de Telecomunicació, Universitat Politécnica de Catalunya, 08034 Barcelona, Spain (e-mail: pradell@tsc.upc.es).

P. de Paco was with the Departamento de Teoría del Senyal i Comunicacions, Escola Técnica Superior d'Enginyeria de Telecomunicació, Universitat Politécnica de Catalunya, 08034 Barcelona, Spain. He is now with the Departament de Telecomunicació i Enginyeria de Sistemas, Universidad Autonoma de Barcelona, 08193 Barcelona, Spain.

Digital Object Identifier 10.1109/TMTT.2005.848815

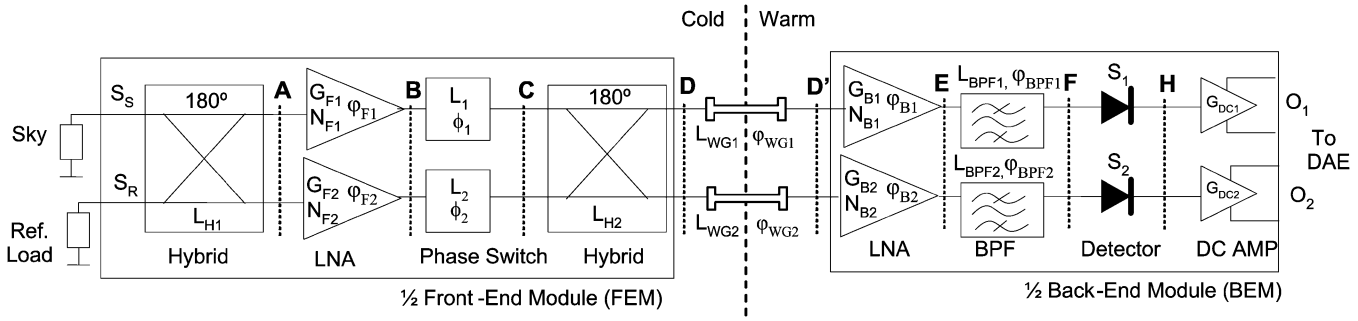

Fig. 2. Half LFI radiometer schematic.

other hand, large bandwidths require a high degree of gain stability of the entire amplifier chain comprising the radiometer. Gain and noise temperature fluctuations of the amplifiers themselves can produce instabilities that reduce the sensitivity. The sensitivity, ΔT, achieved by a radiometer of effective bandwidth β and noise temperature $T_{\rm sys}$ for an integration time τ is given by (1) [6] as follows:

$$\Delta T = T_{\rm sys} \cdot \sqrt{\frac{1}{\beta\tau} + \left(\frac{\Delta G}{G}\right)^2} \tag{1}$$

where $\Delta G/G$ is the mean magnitude of the fractional gain fluctuation with an approximate $1/f$ spectrum frequency [7], [8] occurring during the integration interval and would vanish for an ideal radiometer system. The effective bandwidth of the radiometer β is given by (2) as follows:

$$\beta = \frac{\left[\int_0^\infty G(f)df\right]^2}{\int_0^\infty G^2(f)df} \tag{2}$$

where $G(f)$ is the frequency-dependent power response of the radiometers.

B. Pseudocorrelation Radiometer

The pseudocorrelation radiometer [9]–[12] allows continuous comparison and differencing between two independent observations, therefore, the sensitivity or the minimum detectable signal is improved by a factor of $\sqrt{2}$ compared to the Dicke radiometer scheme.

Fig. 2 shows a detail of a half LFI radiometer. The other half radiometer has an identical schematic.

The sky and reference load are coupled to a low-noise amplifier (LNA), in parallel chains, in the FEM via a 180° hybrid coupler. Each signal then propagates through a phase switch. There are two phase switches to keep symmetry, but only one of them applies a phase shift that changes between 0°–180° at a frequency rate of 4096 Hz. A second 180° hybrid coupler in the FEM recombines the signals and delivers a power proportional to each input load in a different BEM branch. Rapid switching ensures that gain fluctuations in the BEM do not significantly affect the overall radiometer gain stability. In the BEM, signals are amplified, filtered by a bandpass filter, and detected with a square-law detector.

Finally, a low-noise dc amplifier increases the detected signal to the data acquisition electronic module.

The outputs are switched data signals alternately proportional to the sky and reference load temperatures modulated at the frequency of the phase switching. These output signals are integrated and digitized.

The expression of the FEM output signals for each frequency in plane D according to Fig. 2 are given by (3) and (4) as follows:

$$\begin{aligned} D_1 = &-\frac{j}{\sqrt{2}}\left(\frac{G_{F1}}{L_{H1}L_1L_{H2}}\left(\frac{-j(S_S+S_R)}{\sqrt{2}}+N_{F1}\right)\cdot e^{j(\varphi_{F1}+\phi_1)}\right) \\ &-\frac{j}{\sqrt{2}}\left(\frac{G_{F2}}{L_{H1}L_2L_{H2}}\left(\frac{j(S_S-S_R)}{\sqrt{2}}+N_{F2}\right)\cdot e^{j(\varphi_{F2}+\phi_2)}\right) \end{aligned} \tag{3}$$

$$\begin{aligned} D_2 = &\frac{j}{\sqrt{2}}\left(\frac{G_{F1}}{L_{H1}L_1L_{H2}}\left(\frac{-j(S_S+S_R)}{\sqrt{2}}+N_{F1}\right)\cdot e^{j(\varphi_{F1}+\phi_1)}\right) \\ &-\frac{j}{\sqrt{2}}\left(\frac{G_{F2}}{L_{H1}L_2L_{H2}}\left(\frac{j(S_S-S_R)}{\sqrt{2}}+N_{F2}\right)\cdot e^{j(\varphi_{F2}+\phi_2)}\right) \end{aligned} \tag{4}$$

where S_S and S_R are the signals from the sky and reference load, respectively, L_{H1} and L_{H2} are the hybrids' insertion losses, G_{F1}, G_{F2}, N_{F1}, and N_{F2} are the LNA gains and noise in the FEM with phase shifts φ_{F1} and φ_{F1}, L_1 and L_2 are the phase-switch insertion losses, and ϕ_1 and ϕ_2 are the phases of the phase switches.

The BEM outputs O_1 and O_2, according to the nomenclature in Fig. 2, are video voltage signals obtained by integration along the frequency band with (5) and (6), and these voltages take into account the square-law response of the diode detector

$$O_1 = G_{\rm DC1}\cdot\int_{f_1}^{f_2} S_1\cdot\left|\frac{G_{B1}\cdot(D_1+N_{B1})}{L_{\rm WG1}\cdot L_{\rm BPF1}}\right|^2 df \tag{5}$$

$$O_2 = G_{\rm DC2}\cdot\int_{f_1}^{f_2} S_2\cdot\left|\frac{G_{B2}\cdot(D_2+N_{B2})}{L_{\rm WG2}\cdot L_{\rm BPF2}}\right|^2 df \tag{6}$$

where $G_{\rm DC1}$ and $G_{\rm DC1}$ are the dc amplifier gains, and S_1 and S_2 are the sensitivities of the detectors. G_{B1}, G_{B2}, N_{B1}, and N_{B2} are the LNA gains and noise with phases φ_{B1} and φ_{B2}.

L_{WG1}, L_{WG2}, L_{BPF1}, and L_{BPF2} are the waveguides and bandpass filter insertion loss, and their phases are φ_{WG1}, φ_{WG2} and φ_{BPF1}, φ_{BPF2}, respectively. D_1 and D_2, the FEM outputs expressions, are (3) and (4), respectively.

The most important effects are described in the previous analysis to show how each subsystem relates to the overall radiometer performance. Nonidealities in the components comprising the radiometer lead to effects not included in the above expressions.

In order to simplify the equations' insertion losses, gains, noise, and sensitivities are considered to be flat over the band and identical for both branches. The product of gains and insertion losses in the FEM and BEM is denoted G according to (7) as follows:

$$G = \frac{G_F \cdot G_B}{L_F \cdot L_B} \tag{7}$$

where $G_F = G_{F1} = G_{F2}$, $G_B = G_{B1} = G_{B2}$, $L_F = L_{H1} \cdot L_1 \cdot L_{H2} = L_{H1} \cdot L_2 \cdot L_{H2}$, and $L_B = L_{\mathrm{WG1}} \cdot L_{\mathrm{BPF1}} = L_{\mathrm{WG2}} \cdot L_{\mathrm{BPF2}}$.

The phase ϕ_1 will be 0° and ϕ_2 applies a phase shift that changes between 0°–180°, therefore, the output voltage at each branch, considering uncorrelated noise, is given by (8)–(11), respectively.

Case 1) ϕ_1 and ϕ_2 equal to 0°

$$O_1 = G_{\mathrm{DC1}} \cdot S_1 \cdot \left| G \cdot \left(S_R + \frac{2N_F}{\sqrt{2}} + \frac{L_F \cdot N_B}{G_F} \right) \right|^2 \tag{8}$$

$$O_2 = G_{\mathrm{DC2}} \cdot S_2 \cdot \left| G \cdot \left(S_S + \frac{2N_F}{\sqrt{2}} + \frac{L_F \cdot N_B}{G_F} \right) \right|^2. \tag{9}$$

Case 2) ϕ_1 equal to 0° and ϕ_2 equal to 180°

$$O_1 = G_{\mathrm{DC1}} \cdot S_1 \cdot \left| G \cdot \left(S_S + \frac{2N_F}{\sqrt{2}} + \frac{L_F \cdot N_B}{G_F} \right) \right|^2 \tag{10}$$

$$O_2 = G_{\mathrm{DC2}} \cdot S_2 \cdot \left| G \cdot \left(S_R + \frac{2N_F}{\sqrt{2}} + \frac{L_F \cdot N_B}{G_F} \right) \right|^2 \tag{11}$$

where $N_F = N_{F1} = N_{F2}$, $N_B = N_{B1} = N_{B2}$, and $\varphi_1 = \varphi_2 = 0°$.

The output of the radiometer is then the difference of O_1 and O_2 obtained by post-processing. In Section V-E-II, the differential output voltage using temperatures is presented.

An advanced elegant breadboard (EBB) at 30 GHz of the radiometer [13] has been constructed to verify the performance of the system. This prototype radiometer chain has provided knowledge about design and fabrication of critical components, radiometer characterization, systematic errors, and nonidealities [14]. The 30-GHz radiometer design goals and requirements are summarized in Table I. The total microwave gain of each chain in the radiometer was selected in order to have −30 dBm as the input power to each diode detector.

TABLE I
RADIOMETER PERFORMANCE SPECIFICATIONS

Item	Value
Number of feeds	2
Sensitivity	0.17 mK· $\mathrm{Hz}^{-1/2}$
System Noise Temperature	9 K
System 1/f knee frequency	39 mHz
System Isolation	12 dB
System Effective bandwidth	6 GHz
FEM power consumption	27 mW
FEM Gain	30 dB
BEM Gain	30 dB
BEM Noise Temperature	300 K

III. FEM

A half FEM was built as the EBB comprising one input hybrid coupler, two LNAs, two phase switches, and one output hybrid coupler.

A. Hybrid Couplers

Each half FEM has a balanced structure based on two matched magic-T hybrids. The first one provides half of the input power from input loads to each branch. The second one acts as a combiner and delivers a power proportional to each input load to a different BEM branch. Both hybrids have coaxial line probe transitions to WR-28. They have been designed using electromagnetic modeling software and they have been machined from aluminum alloy and gold-plated. The contribution to the system noise of the input hybrid was negligible due to the effect of its waveguide design and the low operating temperature. To integrate the FEM, two identical blocks with two hybrids were built as a single body ready to house the LNAs and phase switches.

B. LNAs

LNAs are key components in millimeter-wave radar and radiometer system applications.

The amplifiers, especially developed for the 30-GHz radiometer receivers, have shown the best noise performance among the reported InP-based LNAs at 20 K.

The designed LNAs have four stages. They have been developed in millimeter-wave microwave integrated-circuit (MIC) technology using InP HEMTs manufactured by NGST (formerly TRW), Redondo Beach, CA. The design has been carried out with available models for all the components used in the amplifiers. From models at room temperature, their performance at cryogenic temperatures have been taken into account, with stability being a critical parameter.

The LNA transistors and matching networks were placed in a narrow width channel in order to avoid oscillations related to waveguide moding. Transistors are connected to microstrip lines made on a Cuflon 0.003-in dielectric constant (ε_r) of 2.2 with gold bonding wires. $\lambda/4$ bond wires connecting the bias lines act like an RF choke. The resistors and capacitors presented in the bias circuitry network are used to assure amplifier stability at low frequencies. Within the band, their effect can be neglected due to the presence of the $\lambda/4$ wire, but outside, they act as stabilizing elements.

The noise temperature requirement of these LNAs was lower than ever previously achieved with a multistage transistor amplifier. They have provided very low noise performance with very low power consumption at cryogenic temperature. The LNA gain was approximately 34.7 dB and pairs of LNAs were

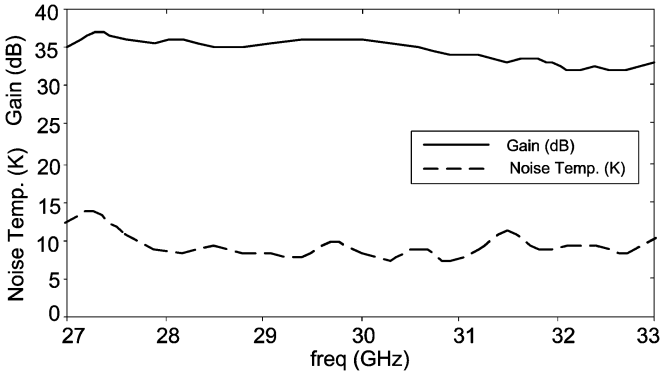

Fig. 3. Measured LNA gain and noise temperature at 15 K.

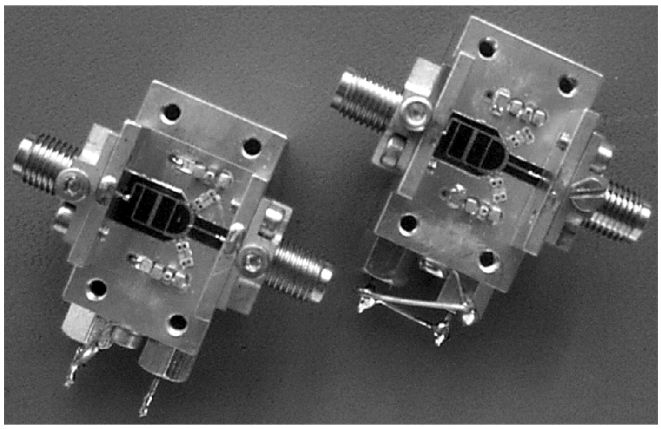

Fig. 4. HEMT-based phase switches, comprising a microstrip hybrid, active devices, and bias circuitry.

matched in gain and phase. The average noise temperature over the 6-GHz bandwidth was 9.4 K at 15 K. These results are among the best reported [15], [16]. The gain in decibels and the noise temperature in kelvin over the operating bandwidth of one LNA is depicted in Fig. 3.

The bias settings for front-end LNAs were set for 20-K operation. The performance was optimized to obtain maximum gain and minimum noise figure. In both amplifiers, all the drain voltages were 0.6 V and the power consumption were calculated to be 10.6 and 10.8 mW.

C. Phase Switch

The phase-switch design has been the subject of an international patent [17] and it has been used on all LFI radiometers. One phase switch [18] is placed in each FEM branch. It connects the LNA outputs to the output hybrid and it introduces a phase shift of 180° in the signal in one state with relation to the other. This circuit has been specially designed for PLANCK LFI at all frequencies. The phase switches used in this EBB FEM assembly were designed with GaAs HEMTs as active elements, leading to a very low power dissipation of a few microwatts. The microstrip lines were made on a Cuflon 0.003-in dielectric constant (ε_r) of 2.2. Two HEMT-based phase switches were assembled and tested at room temperature in a jig shown in Fig. 4. The electronic bias consists of a decoupling.

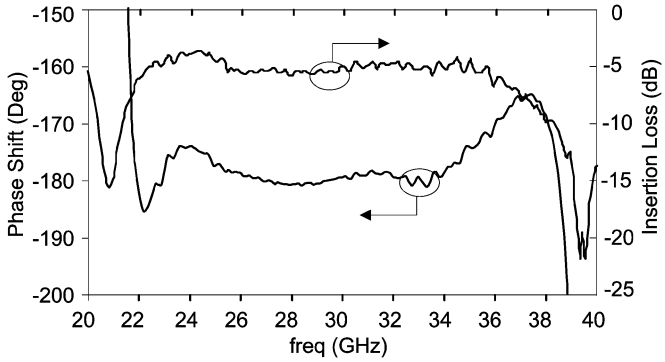

Fig. 5. Phase shift and insertion loss of the phase switch.

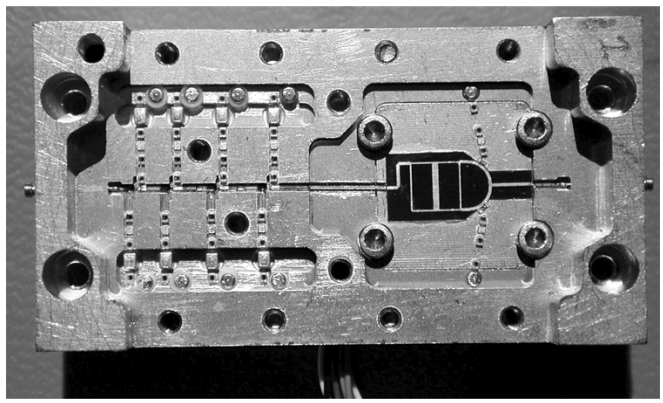

Fig. 6. Part of the EBB FEM showing four-stage LNA- and HEMT-based phase switch.

Phase shift and insertion loss at room temperature are depicted in Fig. 5 showing a very flat response along the operating bandwidth with a peak-to-peak variation of 5° over 10 GHz and 1.5° over a 6-GHz-band circuit formed by capacitors and resistors. The results have shown very wide-band performance for this design of a 180° phase shifter. The insertion loss was 4–6 dB over a 13-GHz band, but it is thought to be partly attributable to the test jig in which the switches were mounted. The only drawback of the phase switch was the relatively high insertion loss $(\sim 6\ \text{dB})$, but its placement after the LNA means it does not have much effect on the system noise temperature.

An improved phase switch designed on an InP monolithic microwave integrated circuit (MMIC) chip version was manufactured on the HBT InP wafer process at NGST. These chips were tested warm and cold and showed to not only have better performance than the other versions, but to offer significant simplification in construction and integration into the FEM. Test results at 30 GHz were excellent, phase response of $180^\circ \pm 1^\circ$, insertion loss lower than 2.5 dB, and return loss better then 10 dB across the operating bandwidth.

D. FEM Branch

An LNA- and HEMT-based phase switch have been assembled in split blocks. Fig. 6 shows one four-stage LNA followed by the phase switch. Two identical blocks were integrated with the hybrids, being part of the FEM body, to build a receiver.

An external view of a half FEM is shown in Fig. 7, depicting the two hybrid input waveguides (WR-28) and mounting lugs.

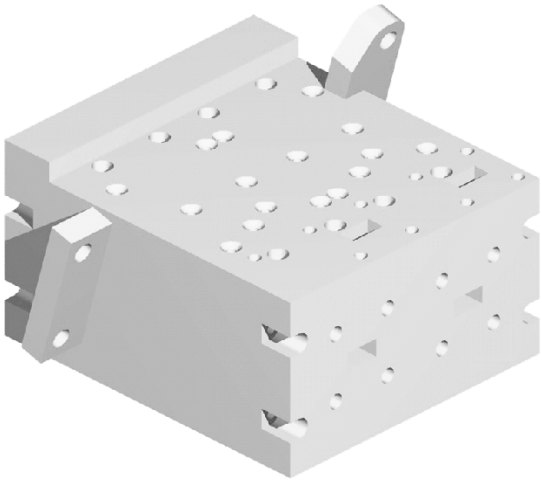

Fig. 7. Exterior of a half FEM, showing input hybrid ports and mounting lugs.

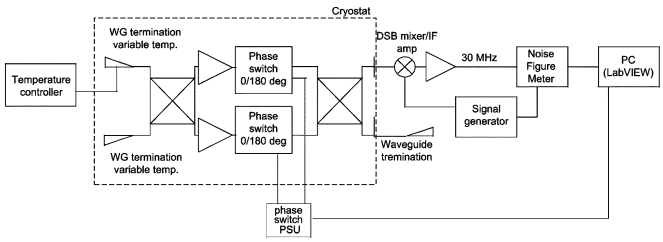

Fig. 8. Setup schematic to test output power.

E. FEM Test and Performance

Firstly, the half FEM was tested at room temperature to indicate whether the FEM is working properly. It does not reveal subtleties of performance, but indicates that the amplifiers and phase switches are still operating with the correct bias conditions. The sky target in these tests was a WR28 waveguide load, and the reference load was a prototype of the 4-K reference load, both at room temperature.

The half FEM was then cooled to 20 K and it was tested. The FEM output power across the band was plotted using a double-sideband mixer, signal generator, and noise-figure meter according to the test setup shown in Fig. 8.

The output power versus frequency in one output of the FEM with the four combinations of the phase-switch state is shown in Fig. 9. The waveguide terminations inside the cryostat were at 100 K as a hot load, and at 17.3 K as a cold load.

Both traces in Fig. 9 with higher output power belong to the cases 180° and 0° or 0° and 180° phase-switch states and these are related to the 100-K load temperature. When both phase switches have the same state, the output power is lower and related to 17.3 K. The results for the other output in the FEM were very similar, but the same levels of output power are obtained with opposite phase-switch states.

IV. BEM

The BEM, where signals are amplified, filtered, and detected has RF inputs and dc outputs. The half BEM is composed of two identical branches and each one comprises two LNAs, one bandpass filter, a diode detector, and a dc amplifier. The BEM gain is specified to be 30 dB in order to have the detector diode working

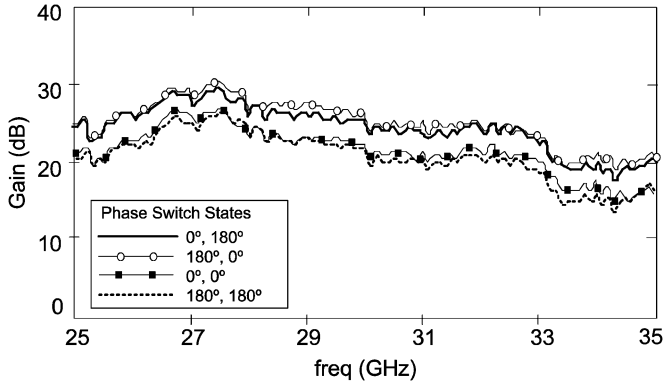

Fig. 9. FEM gain versus frequency for various phase-switch states.

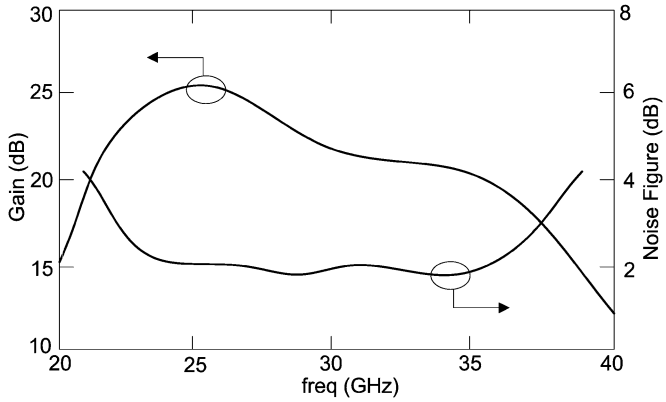

Fig. 10. LNA noise figure and gain at room temperature.

in its linear region. Two identical MMIC LNAs have been cascaded in order to provide the necessary gain. A WR-28 waveguide-to-microstrip transition was designed using a stepped-ridge waveguide and it is the first functional element of the BEM. This transition has been chosen for its broad bandwidth, low insertion loss, and repeatable performance.

A. LNA

The LNA is on MMIC technology. The operating frequency range of the amplifier is greater than the required bandwidth of the BEM. The selected MMIC amplifier was the model HMC263 from Hittitem, Chelmsford, MA. It is a high-gain broad-band four-stage monolithic LNA, which covers the frequency range of 24–36 GHz, and its size is 3.29 mm^2. The chip utilizes a GaAs pseudomorphic high electron-mobility transistor (pHEMT) process offering a noise figure and a gain against frequency from a single bias supply of +3 V @ 37 mA, as depicted in Fig. 10.

B. Bandpass Filter

A bandpass filter was used to define an effective bandwidth of 20% and to reject undesired radiation out of the band of interest. Low bandpass losses, more than 10 dB out-of-band losses, and small size were considered the main objectives. A microstrip coupled-line topology was chosen because it provides inherently bandpass characteristics. A three-resonator filter has been designed using the design method from the classic prototype filter tables proposed in [19] and a design methodology has

Fig. 11. 30-GHz bandpass filter on Duroid 6002.

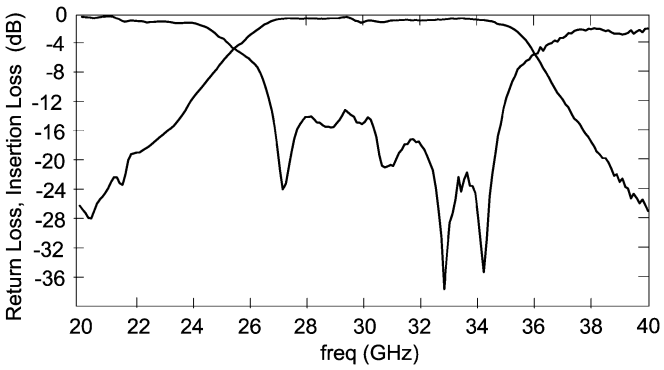

Fig. 12. Insertion and return losses of the bandpass filter.

been developed to achieve predictable frequency response in microstrip filters using a commercial computer-aided design (CAD) software. After a careful evaluation of the validity of the CAD models, comparing simulated and accurately measured results, the design was restricted to microstrip elements that can be well characterized [20].

The selection of the substrate becomes critical due to the gaps and widths of microstrip lines because it sets the line-etching precision required and the minimum losses achievable. The filter in Fig. 11 has been fabricated on a Duroid 6002 substrate with 0.254-mm thickness and dielectric constant (ε_r) of 2.94.

Fig. 12 shows the filter response when it is measured with coplanar-to-microstrip transitions on a coplanar probe station. The insertion losses were lower than 1.5 dB in the whole band, and the return losses were better than 12 dB.

C. Detector

After the signal is amplified and filtered, a square-law detector is used to convert the signal from the sky or from the reference load to dc voltage.

The detector is composed of a hybrid reactive/passive matching network and a low-barrier Schottky diode. A beam-lead zero-bias diode, model HSCH-9161, was selected.

A large- and small-signal diode model have been developed to optimize the design. The matching network design requires additional lossy components to meet the system requirements. It uses a 100-Ω-thick film resistor and its nonideal behavior at the millimeter frequency band was included in the simulations of the matching network. A radial stub is used to provide RF ground to the diode. The virtual ground was also used to extract the dc output voltage and a dc return was provided by the 100-Ω resistor ground connection. A 100-kΩ load resistor was used as video impedance to extract the detected voltage. The detector circuit was implemented on an alumina dielectric substrate ($\varepsilon_r = 9.9$; thickness $= 0.254$ mm). This detector, shown in Fig. 13, has been characterized individually on a coplanar probe station with coplanar-to-microstrip transitions.

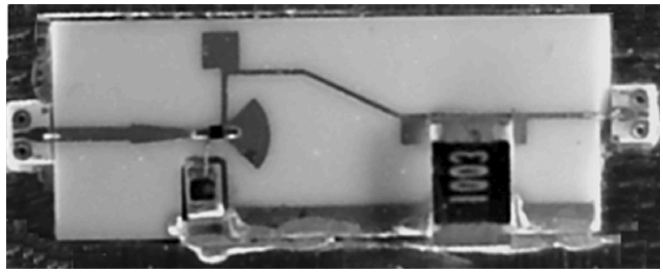

Fig. 13. 30-GHz diode detector. From the left-hand side: matching network including 100-Ω resistor, diode connected to radial stub, and 100 kΩ at the output.

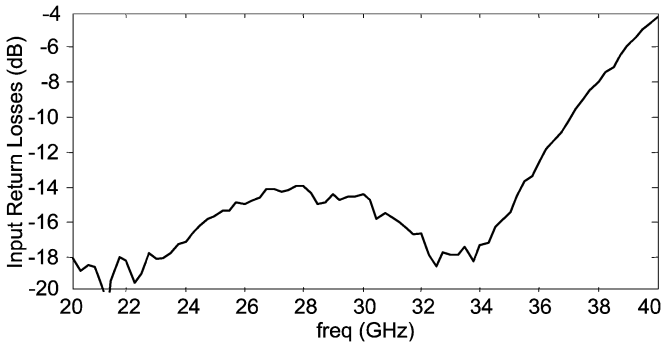

Fig. 14. Detector input return loss for an input power of -30 dBm.

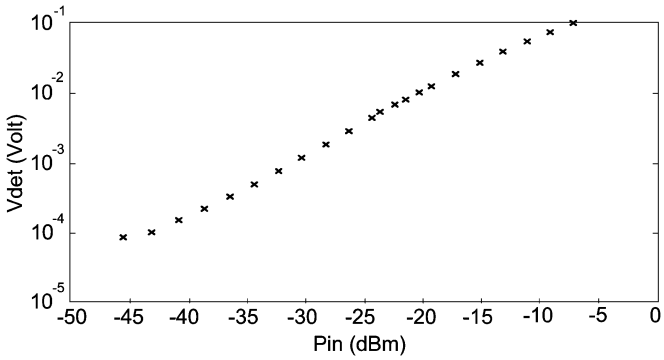

Fig. 15. Detector output voltage versus input power at 30 GHz.

The input return loss measured with -30-dBm input power using a vectorial network analyzer (HP8510C) is depicted in Fig. 14.

The rectification efficiency or output voltage sensitivity versus input power was measured at three frequencies across the band 27, 30, and 33 GHz. Detector sensitivity curve at 30 GHz has been included in Fig. 15, showing linear performance around -30 dBm of input power and a rectification efficiency around 1000 mV/mW. Dynamic range for quadratic response covers from -40 to $-$ 15 dBm.

D. DC Amplifier

In order to provide sufficient detected signal to the data acquisition electronic module, a low-noise dc amplifier has been designed. A schematic of the dc amplifier is shown in Fig. 16.

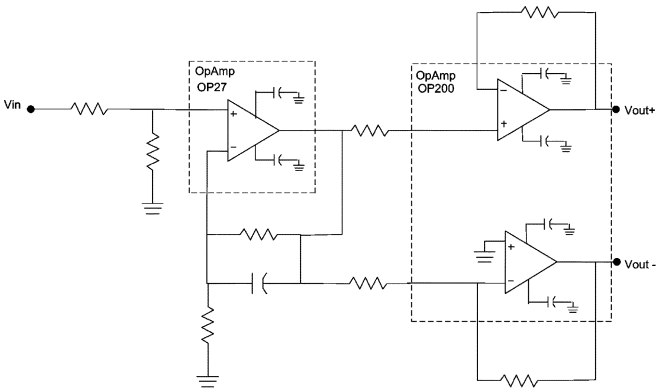

Fig. 16. DC amplifier.

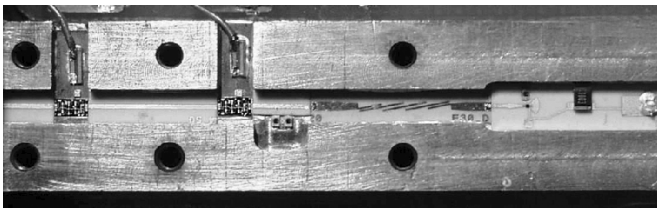

Fig. 17. Branch of the BEM.

The first stage has an OP27 precision operational amplifier that combines low offset and drift characteristics with low noise, making it ideal for precision instrumentation applications and accurate amplification of a low-level signal. A second balanced stage, implemented with a IC-OP200, provides a balanced and bipolar output. DC amplifier total power consumption with a high-impedance load is approximately 37 mW.

E. Branch of the BEM

In order to have the EBB, two identical branches were built, and one of them is shown in Fig. 17. From the left- to right-hand side in the branch, there are two MMIC LNAs interconnected by microstrip transmission lines on an Al_2O_3 substrate, 0.254-mm thick, a relative dielectric constant of 9.9, the bandpass filter using microstrip coupled lines on the PTFE-based substrate, and the microstrip Schottky diode detector.

The EBB BEM has two identical branches with a WR-28 waveguide input and dc output connector.

F. BEM Test and Performance

Tests of the half BEM have been done at room temperature. Fig. 18 shows the detected voltage of the two branches, sweeping the frequency with a signal generator from 22 to 40 GHz when a constant power level above the white noise power is applied. The input power was -60 dBm, which is similar to the noise power output from the FEM.

V. Radiometer Performance and Results

The FEM and BEM were connected with a 1–m-long waveguide. Tests of linearity, system noise temperature, leakage, gain, effective bandwidth, and $1/f$ knee frequency were carried out when the FEM was operating at 20 K and the BEM was operating at 300 K. The block diagram in Fig. 19 shows the

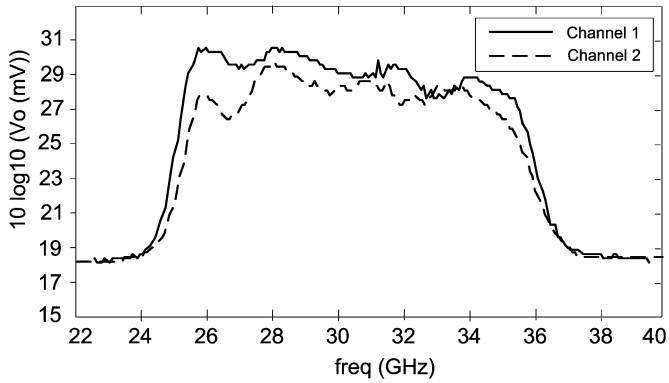

Fig. 18. RF to dc responses of the half BEM.

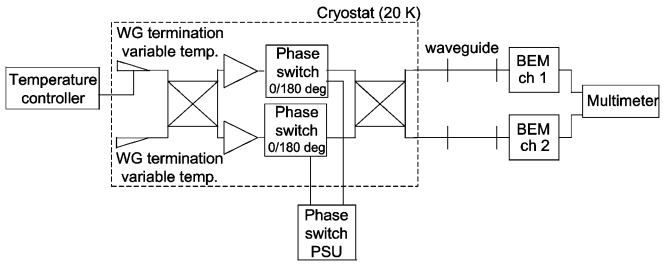

Fig. 19. Test setup.

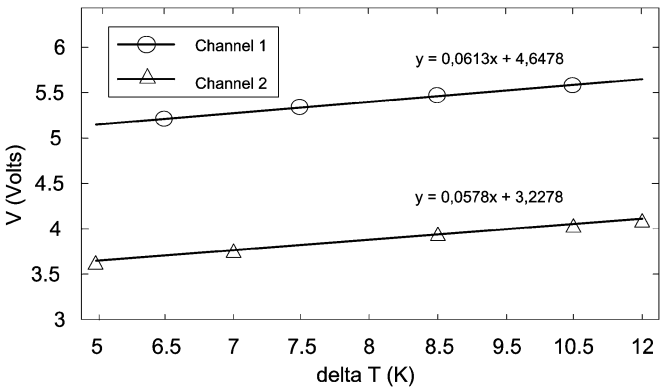

Fig. 20. Radiometer calibration curves.

configuration of the radiometer to perform some of the measurements. Test of $1/f$ spectrum and effective bandwidth were carried out with a test setup slightly different than that shown Section V-A.

The FEM with the input hybrid, LNAs, phase switches, and output hybrid are cooled to approximately 20 K in the cryostat. Noise inputs come from two WR-28 terminations, both cooled, but one is temperature controlled so that accurate temperature differentials can be set between the input terminations for calibration and test purposes.

A. Radiometer Operation

1) Linearity, Calibration Curve: In order to calculate the radiometer constant, a calibration curve was calculated. The temperature of the hot load was varied. Corresponding voltages at the video amplifier output were measured by taking 1-s runs of the switched radiometer at each new temperature, and calculating the mean of the resulting time series. Fig. 20 shows a

graph of voltage (V) versus temperature increment (ΔT) at various temperatures for both radiometer channels.

The straight line indicates the linearity of the detectors. Using the equation of the line, the radiometer constant can be determined as $1/0.0613 = 16.31$ K/V and $1/0.0578 = 17.54$ K/V for each BEM channel.

The calibration constant can also be determined by increasing the temperature during the recording of a 5–min switched data run. The beginning and end levels of the resulting ramp in the time series yield an immediate ΔV value for the ΔT increment. The two values obtained for the differential calibration constant were 16.3 K/V for BEM channel 1 and 17.3 K/V for BEM channel 2.

B. Leakage and System Noise Temperature

Leakage is a measure of the detected energy from the sky into the detected output from the reference termination and vice versa. It is required to be less than 10%. It is minimized by accurately matching the phase and amplitude responses of the LNA and phase-switch pairs.

In order to measure the leakage and system noise temperature, the detected outputs in each switched state were compared. A multimeter was used to measure the detected voltages from the BEM for the four phase-switch settings. The test involved measuring the detected outputs in each switched state with both input terminations at minimum temperature, then heating one of the terminations and re-measuring the detected voltages to determine the Y-factor. In an ideal system, two phase-switch settings 0°, 0° and 180°, 180° would connect hot temperature input termination $T_{\rm hot}$ to the output and the cold temperature load $T_{\rm cold}$ would be connected via phase-switch settings 0°, 180° and 180°, 0°. However, there is leakage between the states.

To measure the leakage and noise temperature of the individual branches, the temperature of $T_{\rm hot}$ was raised and, in the process, a small increment was applied to $T_{\rm cold}$. Therefore, there are two hot temperatures and two cold temperatures that are applied to the radiometer. The output detected voltages proportional to the input temperatures with all the phase-switch settings are measured to obtain four Y-factors, two per branch, as in (12) and (13) as follows:

$$Y_1 = \frac{V_{\rm hot1}}{V_{\rm hot2}} \tag{12}$$

$$Y_2 = \frac{V_{\rm cold1}}{V_{\rm cold2}} \tag{13}$$

where $V_{\rm hot1}$ and $V_{\rm hot2}$ are the output voltages in pair 0° or 180° of phase-switch settings, $V_{\rm cold1}$ and $V_{\rm cold2}$ are the output voltages in 0°,180° or 180°, 0°.

The Y-factors for one branch allow us to calculate the system noise temperature and the leakage substituting in (14) and (15) as follows:

$$Y_1 = \frac{T_{\rm sys} + T_{\rm hot1}(1-L) + T_{\rm cold1}L}{T_{\rm sys} + T_{\rm hot2}(1-L) + T_{\rm cold2}L} \tag{14}$$

$$Y_2 = \frac{T_{\rm sys} + T_{\rm cold1}(1-L) + T_{\rm hot1}L}{T_{\rm sys} + T_{\rm cold2}(1-L) + T_{\rm hot2}L} \tag{15}$$

TABLE II
Y-FACTORS, LEAKAGE, AND NOISE TEMPERATURE

Switch State (Φ_1, Φ_2)	T_{hot1} = 50 K, T_{cold1} = 17.24 K, T_{hot2} = 17.71 K, T_{cold2} =13.8 K	
	Out1	Out 2
180°,180°	Y_1=2.13	Y_2=1.23
0°,180°	Y_2=1.22	Y_1=2.07
	T_{sys} = 9.3 K	T_{sys} = 10.6 K
	L = 6.2 %	L = 7.8 %

TABLE III
SYSTEM NOISE TEMPERATURE

Physical Temp (K)	System Noise Temp (K)	Accuracy (± K)
60	19	5.7
30	10.2	4.2
20	9.1	2.7

where $T_{\rm sys}$ is the system noise temperature, $T_{\rm hot1}$ is the highest temperature of hot load, and $T_{\rm hot2}$ is the lowest in pair 0° or 180°, $T_{\rm cold1}$, $T_{\rm cold2}$ are the temperature of cold load in pair 0°,180° or 180°, 0°, and L is the leakage.

Two pairs of phase-switch state (0°, 0° and 180°,180°, and 0°, 180° and 180°, 0°) share the same leakage due to the amplitude and phase mismatch. Therefore, these numbers can be used to calculate two similar noise temperatures and leakage values per branch. These results are shown in Table II.

Output detected voltage measurements were also performed to estimate the system noise temperature at three different temperatures and the results with their accuracy are presented in Table III.

System noise temperature and leakage were measured in two different ways and the second method used a noise figure meter setup without diode detectors in the BEM. Power readings were taken with 100-MHz steps and averaged across the band. The hot and cold waveguide termination temperatures ($T_{\rm hot1}$, $T_{\rm hot2}$, $T_{\rm cold1}$ and $T_{\rm cold1}$) that appear in Table II were used. This method is based on power measurements through the Y-factors, as in (14) and (15). System equivalent noise temperature and leakage versus frequency are depicted in Fig. 21. The noise temperature is believed to be accurate to approximately ± 2 K. Results of this swept-frequency method agree well with the total power results, shown in Tables II and III.

C. Data-Acquisition System

A data-acquisition system was used to take data over a period of time in order to obtain the output noise spectra. Results of effective bandwidth and $1/f$ output spectrum were obtained using this setup. Fig. 22 shows a schematic diagram of the acquisition system for the 30-GHz EBB.

The FEM under test is placed in a cryogenically cooled environment and kept at 20 K. It is connected to the BEM that has two inputs and two outputs, which relate to a single polarization of the FEM, by two 1-m-long waveguides. A Lakeshore proportional integral derivative (PID) temperature controller is used to control the FEM and waveguide termination temperatures, as well as providing temperature monitoring. The phase-switch drive signal is sent to driver hardware in the FEM bias supply box so that each phase switch can be switched or set to either

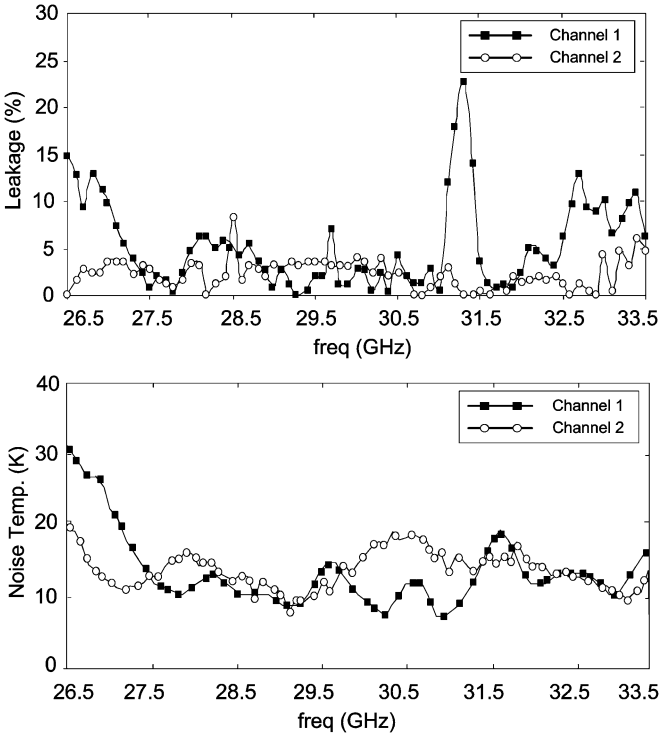

Fig. 21. Leakage and noise temperature versus frequency.

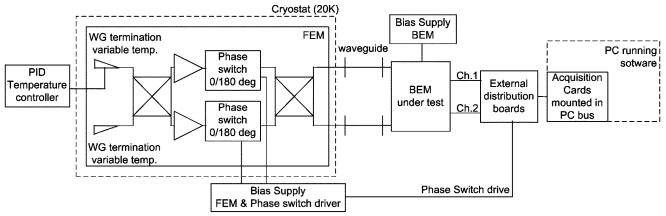

Fig. 22. Scheme of the test setup for data-acquisition system.

the ON or OFF state. Independent drive can be supplied to each of the two phase switches.

Each BEM has two outputs, the positive and negative sides of a balanced output, which is fed to the distribution board.

The acquisition system was controlled by Labview software. Two acquisition cards were mounted on the PC bus, one for the analog-to-digital converters (ADCs) and the other for the digital-to-analog converters (DACs). The acquisition and phase-switch waveforms were synchronized. The hardware connections were made on separate external distribution boards.

A low-pass filter comprised of a resistor and capacitor was used as an integrator. Fig. 23 shows the simple *RC* network that was built into the distribution board for the ADC inputs. It can be seen that channel 1 (CH1) and channel 2 (CH2) are fed into the distribution board as differential inputs and each is presented with a series resistor of 150 Ω and a parallel capacitor of 0.22 μF. The outputs are fed into the differential ADC inputs of the acquisition card.

This built *RC* filter has an equivalent integration time (τ) (16) of twice the theoretical *RC* time response and it is equal to 66 μs as follows:

$$\tau = 2 \cdot R \cdot C. \tag{16}$$

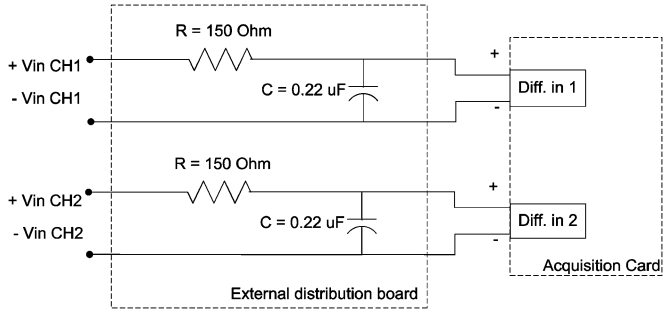

Fig. 23. Schematic diagram of the *RC* networks built into the external distribution board.

The low-pass filter 3-dB bandwidth $B_{3\ \mathrm{dB}}$ is defined as follows in (17):

$$B_{3\ \mathrm{dB}} = \frac{B_{\mathrm{eq}}}{1.57} = \frac{1}{(1.57 \cdot 2 \cdot \tau)} \tag{17}$$

where B_{eq} is the postdetection equivalent bandwidth.

The designed low-pass filter has a 4.8-kHz 3-dB bandwidth and a 7.5-kHz postdetection equivalent bandwidth. The half-power bandwidth determines the acquisition sample rate when the filter response is sharp. In the case of the simple *RC* filter used, the more appropriate sample rate is that related to the post-detection equivalent bandwidth since, beyond 3-dB bandwidth, there is power and the optimum sample rate is that which covers the highest frequency entering to the acquisition system. Therefore, this implies a sample rate of around 15 kHz.

The switching frequency of the switches was set to 280 Hz and the sampling rate to 16.8 kHz, being a multiple of the phase-switch rate, and then re-sampled. For testing purposes, a switch rate of 280 Hz, lower than the baseline of 4096 Hz, was chosen to limit the sampling rate while providing enough samples of each switch state in the data streams to avoid losing accuracy.

D. Effective Bandwidth

The effective bandwidth [6] of both branches was calculated from the total power radiometer expression (18) as follows:

$$\frac{\Delta T}{T_{\mathrm{sys}}} = \frac{\Delta V}{V} = \frac{1}{\sqrt{\beta \tau}} \tag{18}$$

where ΔT is the sensitivity of the radiometer, T_{sys} is its equivalent noise temperature, β is the effective bandwidth, τ is the integration time, ΔV is the rms value of output voltage noise, and V is the dc output detected voltage.

Measurements of the dc output detected voltage and the rms value of the output voltage noise were taken in all four switched states for both branches, respectively. The appropriate sample rate was used in order to calculate the effective bandwidth with the acquisition system shown in Fig. 22 and with the integrator in Fig. 23. Unswitched data over a period of time were taken in order to know the white noise level of the output noise spectrum.

The effective bandwidths for both "high" states, or the states where the output voltage corresponds to the highest temperature termination, in both branches were calculated and the results are shown in Table IV. The level in $\mathrm{V_{rms}}$ is determined by taking a

TABLE IV
EFFECTIVE BANDWIDTH

Branch output	Switch State (Φ_1, Φ_2)	V (Volt)	ΔV (V_{rms})	β (GHz)
1	180°,180°	4.95	$7.13 \cdot 10^{-3}$	7.3
2	0°,180°	3.51	$5.57 \cdot 10^{-3}$	6.0

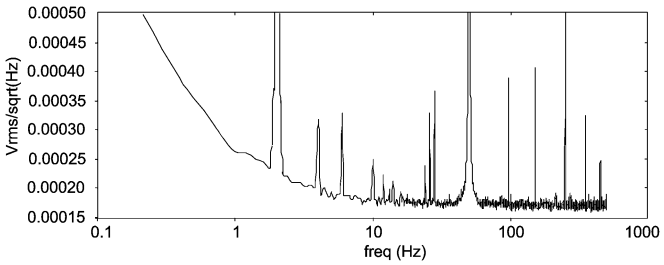

Fig. 24. Unswitched power spectrum.

mean in a section of white noise in the bandwidth of the low-pass filter.

The effective bandwidth achieved was consistent with the 20% specification for the radiometer.

E. Stability

In coherent radiometric systems, one of the major concerns is presented by gain and noise temperature fluctuations of the amplifiers. Since the sensitivity is reduced, the receiver noise performance is degraded and spurious correlations in the measured maps are introduced [21].

The schematic diagram of the acquisition system shown in Fig. 22 with the integrator in Fig. 23 were used to take unswitched and switched data over a period of time in order to obtain the output noise spectrum.

1) $1/f$ Knee Frequency: The frequency at which the gain fluctuations contribute a variance to the output of a total power radiometer equal to that resulting from the system noise temperature is parameterized as the $1/f$ knee frequency.

The white noise level in $V_{rms}/\sqrt{(Hz)}$ is determined by taking the mean of the fast Fourier transform (FFT) in a quiet section well away from the $1/f$ region

To obtain a power spectrum with sufficient resolution to define the $1/f$ knee frequency, it is necessary to take a data run over at least 10 min. Both unswitched and switched runs were taken to demonstrate the improvement in knee frequency achieved with switching.

Unchopped data were collected for 83 min, sampling at 16 800 samples/s, and the power spectrum is shown in Fig. 24. If the data were not switched, the $1/f$ knee frequency was approximately 4 Hz, and the white noise approximately 0.17 $mV_{rms}/\sqrt{(Hz)}$. The noise power spectrum for the other channel was very similar with a $1/f$ noise cutting into the white noise limit at approximately the same frequency.

To obtain the switched power spectrum, the switching frequency was set to 280 Hz and it was a square waveform. One of the phase switches is switched at 280 Hz and the other is fixed in one state. This switch rate is slower than 4096 Hz and cannot avoid the faster variations of gain and noise temperature in the BEM. However, the results are valuable because they confirm

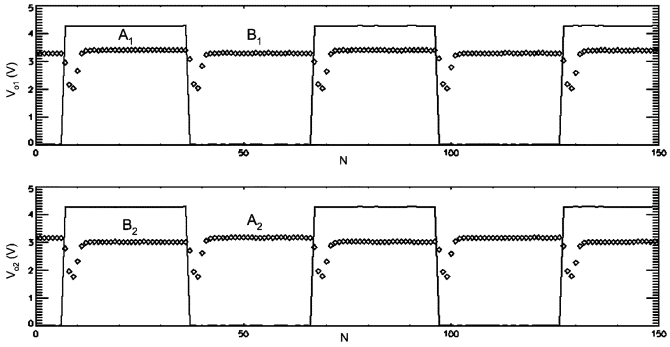

Fig. 25. Switched data stream from each channel (circles), phase-switch driving signal (solid line).

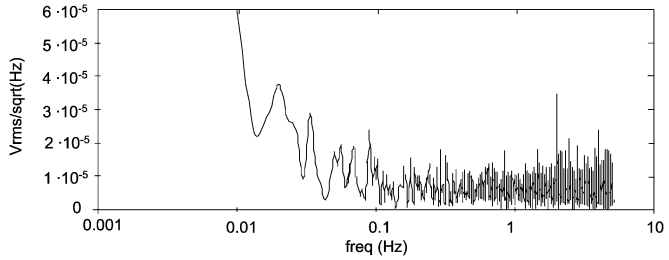

Fig. 26. Switched power spectrum.

that the $1/f$ knee frequency in the BEM is lower than 280 Hz and the radiometer is insensitive to its fluctuations. Data were taken for a period of 15 min and sampling at 16 800 samples/s. Fig. 25 shows switched data stream from each channel.

The voltage levels in the output data stream for each phase-switch state have been identified as A1, B1 for channel 1 and A2, B2 for channel 2. After any phase transition, there is a spike in the data that corresponds to a change in output power as the phase-switch transits. This spike was removed by discarding 20% of the data (10% from each side of the square wave). The time series data were generated by differencing the output data as follows in (19), then a standard FFT routine was used to determine the frequency spectrum and, hence, the $1/f$ knee frequency:

$$(B_2 - A_2) - (B_1 - A_1). \tag{19}$$

The output power spectrum is shown in Fig. 26. The $1/f$ knee frequency was estimated to be approximately 50 mHz.

2) Gain Modulation Factor r: The radiometers measure differences between the sky noise temperature and the reference load at 4 K. It is desirable to minimize the offset between the sky and reference signals in order to reduce instabilities.

The difference between both noise temperatures is compensated to balance the output through the gain modulation factor r [22], [23]. The aim is to maintain the output power as close as possible to zero applying by software the gain modulation factor. The differential output voltage can be written as follows in (20):

$$V_{\text{out}} = S \cdot G \cdot k \cdot \beta \cdot \left(T_{\text{sky}} + T_{\text{sys}} - r(T_{\text{ref}} + T_{\text{sys}})\right) \tag{20}$$

where S is the sensitivity of the detector, G is the radiometer RF gain, k is the Boltzmann constant, β is the bandwidth, T_{sky}

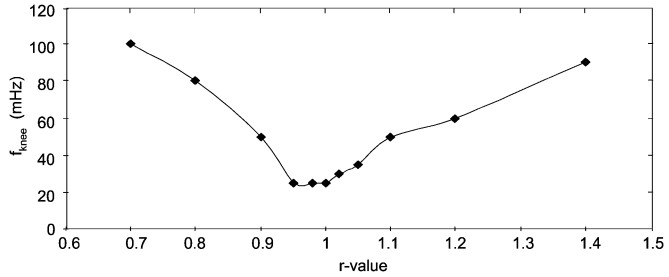

Fig. 27. Variation in knee frequency with r-value.

is the sky temperature, $T_{\rm ref}$ is the reference load temperature, r is the gain modulation factor, and $T_{\rm sys}$ is the system noise temperature. Both $T_{\rm sky}$ and $T_{\rm ref}$ have included contributions due to the antenna insertion loss.

To have an output voltage null by processing the gain modulation factor from (20) can be written as follows in (21):

$$r = \frac{(T_{\rm sys} + T_{\rm sky})}{(T_{\rm sys} + T_{\rm ref})}. \tag{21}$$

The voltage levels from the two branches of the BEM are currently not matched. An r-value is needed to take into account the different levels of $1/f$ noise in each channel in order to have a null output voltage. Therefore, an r-value is assigned to each output channel and calculated using (22) and (23) as follows:

$$(A_1 - r_{x1} \cdot B_1) \tag{22}$$

$$(r_{x2} \cdot B_2 - A_2) \tag{23}$$

where A_1, B_1 are levels of voltage for channel 1 and A_2, B_2 are levels of voltage for channel 2 at each phase-switch state.

Ideally, r_{x1} and r_{x2} would be the same, meaning the two output channels are very similar. A third r-value may be needed when we obtain difference across the diodes and the expression to calculate the time series to obtain frequency spectrum is as follows in (24):

$$(A_1 - r_{x1} \cdot B_1) - r_{x3} \cdot (r_{x2} \cdot B_2 - A_2). \tag{24}$$

The outputs were balanced in hardware using attenuators in order to have r_{x1} and r_{x2} equal. Ignoring the third r-value r_{x3} and applying a single r-value for r_{x1} and r_{x2}, a plot of knee frequency versus r-value was obtained, as shown in Fig. 27.

Using the above optimum r-value of 0.98, the knee frequency was reduced to approximately 30 mHz.

The results demonstrate that the pseudocorrelation radiometer scheme reduces the effect of instabilities of gain and noise temperature. Therefore, by applying an accurate gain modulation factor, a minimization of the $1/f$ knee frequency can be achieved.

VI. Conclusion

Development of microwave hardware for the PLANCK explorer LFI has presented a number of tough challenges to hardware designers. This paper has described the overall system architecture, and the design, assembly, and performance characterization of the 30-GHz EBB differential radiometer for the PLANCK LFI. This is an integrated version of the 30-GHz PLANCK radiometer using two branches of the FEM (at 20 K) and BEM (at 300 K), connected via 1-m-long waveguides. The radiometer operation has been demonstrated successfully, and the overall system noise temperature, gain, effective bandwidth, and $1/f$ noise cancellation have been shown to meet the stringent PLANCK LFI requirements. Instabilities from gain and noise fluctuations have been minimized through the use of phase switching and a gain modulation factor. The performance of the EBB radiometer was excellent: average noise temperature was approximately 9 K over the 20% bandwidth, and the $1/f$ knee frequency was around 30 mHz, demonstrating excellent gain and noise stability.

Acknowledgment

The authors would like to thank the assistance and support of all those who contributed to assemble all the subsystems. The radiometer presented in this paper is the result of many dedicated people to its development.

References

[1] M. Bersanelli, N. Mandolesi, and J. Marti-Canales, "Multi-band radiometer for measuring the cosmic microwave background," in *Proc. 32nd Eur. Microwave Conf.*, Milan, Italy, Sep. 2002, pp. 547–550.

[2] P. Sjoman, T. Ruokokoski, P. Jukkala, and P. Eskelinen, "PLANCK satellite 70 GHz receiver noise test," *IEEE Aerosp. Electron. Syst. Mag.*, vol. 16, no. 12, pp. 19–23, Dec. 2001.

[3] P. Sjoman, T. Ruokokoski, N. J. Hughes, P. Jukkala, P. Kangaslahti, S. Ovaska, and P. Eskelinen, "PLANCK satellite 70 GHz EBB-version back end module," *IEEE Aerosp. Electron. Syst. Mag.*, vol. 18, no. 5, pp. 22–25, May 2003.

[4] C. G. Gentili, R. Nesti, G. Pelosi, and V. Natale, "Compact dual-profiled corrugated circular waveguide horn," *Electron. Lett.*, vol. 36, no. 6, pp. 486–487, Mar. 2000.

[5] G. Morgante, D. Barber, P. Bhandari, R. C. Bowman, P. Cowgill, D. Crumb, T. Loc, A. Nash, D. Pearson, M. Prina, A. Sirbi, M. Schemlzel, R. Sugimura, and L. A. Wade, "Two hydrogen sorption cryocoolers for the PLANCK mission," in *Proc. AIP Conf.*, vol. 616(1), May 2002, pp. 298–302.

[6] J. D. Kraus, *Radio Astronomy*, 2nd ed. Powell, OH: Cygnus-Quasar, 1986.

[7] E. W. Wollack and M. W. Pospieszalski, "Characteristics of broad-band InP millimeter-wave amplifiers for radiometry," in *IEEE MTT-S Int. Microwave Symp. Dig.*, vol. 2, Jun. 1998, pp. 669–672.

[8] N. C. Jarosik, "Measurements of the low-frequency-gain fluctuations of a 30-GHz high-electron-mobility-transistor cryogenic amplifier," *IEEE Trans. Microw. Theory Tech.*, vol. 44, no. 2, pp. 193–197, Feb. 1996.

[9] E. J. Blum, "Sensibilité des radiotélescopes et récepteurs à corrélation," *Annales d'Astrophys.*, vol. 22, pp. 140–163, Feb. 1959.

[10] K. Fujimoto, "On the correlation radiometer technique," *IEEE Trans. Microw. Theory Tech.*, vol. MTT-12, no. 2, pp. 203–212, Mar. 1964.

[11] M. E. Tiuri, "Radio astronomy receivers," *IEEE Trans. Antennas Propag.*, vol. AP-12, no. 12, pp. 930–938, Dec. 1964.

[12] C. R. Predmore, N. R. Erickson, G. R. Huguenin, and P. F. Goldsmith, "A continuous comparison radiometer at 97 GHz," *IEEE Trans. Microw. Theory Tech.*, vol. MTT-33, no. 1, pp. 44–51, Jan. 1985.

[13] B. Aja, E. Artal, L. de la Fuente, J. P. Pascual, A. Mediavilla, N. Roddis, D. Kettle, F. Winder, L. Pradell, and P. De Paco, "Very low noise differential radiometer at 30 GHz," in *Proc. 34th Eur. Microwave Conf.*, Amsterdam, The Netherlands, Oct. 2004, pp. 749–752.

[14] A. Mennella, M. Bersanelli, C. Burigana, D. Maino, N. Mandolesi, G. Morgante, and G. Stanghellini, "PLANCK: Systematic effects induced by periodic fluctuations of arbitrary shape," *Astron. Astrophys.*, vol. 384, pp. 736–742, Mar. 2002.

[15] J. J. Bautista, J. G. Bowen, J. E. Fernandez, B. Fijiware, J. Loreman, S. Petty, and J. L. Prater, "Cryogenic, X-band and Ka-band InP HEMT based LNA's for the deep space network," in *IEEE Aerospace Conf.*, Big Sky, MT, Mar. 2001, pp. 829–842.

[16] A. Cremonini, L. Carbonaro, S. Mariotti, V. Natale, R. Nesti, S. Orfei, J. Roda, and G. Tofani, "Indium phosphide MMIC low noise amplifier and related cyogenically applications in radioastronomical focal plane array receiver," in *Proc. 12th GaAs Symp.*, Amsterdam, The Netherlands, Oct. 2004, pp. 363–366.

[17] R. J. Hoyland, "A wide-band 180° microwave phase shift structure," Patent PCT ESO 1/00 135, 2000.

[18] ——, "A new MMIC, wide-band 180° phase switch design for millimeter wave applications," in *Proc. 3rd ESA Millimeter Wave Technology and Applications Workshop*, Espoo, Finland, May 2003, pp. 305–310.

[19] G. Matthaei, L. Young, and E. M. T. Jones, *Microwave Filters Impedance-Matching Networks, and Coupling Structures*. Norwood, MA: Artech House, 1964.

[20] M. Detratti, B. Aja, J. P. Pascual, M. L. de la Fuente, and E. Artal, "Millimeter wave broad-band bandpass microstrip filters: Design and test," in *Proc. 32nd Eur. Microwave Conf.*, Milan, Italy, Sep. 2002, pp. 573–575.

[21] N. R. Erickson, R. M. Grosslein, R. B. Erickson, and S. Weinreb, "A cryogenic focal array for 85–115 GHz using MMIC preamplifiers," *IEEE Trans. Microw. Theory Tech.*, vol. 47, no. 12, pp. 2212–2219, Dec. 1999.

[22] J. Tuovinen, M. Bersanelli, and N. Mandolesi, "Ultra low-noise and high stability receivers of PLANCK LFI," *Astron. Astrophys.*, vol. 19, pp. 551–558, 2000.

[23] A. Mennella, M. Bersanelli, M. Seiffert, D. Kettle, N. Roddis, A. Wilkinson, and P. Meinhold, "Offset balancing in pseudo-correlation radiometers for CMB measurements," *Astron. Astrophys.*, vol. 410, pp. 1089–1100, Nov. 2003.

Beatriz Aja (S'01) was born in Santander, Spain. She received the Telecommunications Engineering degree from the Universidad de Cantabria, Santander, Spain, in 1999, and is currently working toward the Ph.D. degree at the Universidad de Cantabria.

She collaborates in the development of the BEM at 30 GHz; 44 GHz of the differential radiometers in the European Scientific mission PLANCK. Her areas of interest include the analysis, design, and testing of microwave circuits.

Eduardo Artal (M'80) received the Engineer and Dr. Engineer in telecommunication degrees from the Universitat Politécnica de Catalunya, Barcelona, Spain, in 1976 and 1982, respectively.

From 1976 to 1990, he was an Assistant Professor with the Universitat Politécnica de Catalunya. From 1979 to 1981, while on a partial leave from the Universitat Politécnica de Catalunya, he joined Mier Allende S.A., Barcelona, Spain, where he was involved with TV and FM radio re-emitters development. Since 1990, he has been a Professor with the Universidad de Cantabria, Santander, Spain, where he was Manager of the Telecommunication Engineering course from 1990 to 1994. From 1994 to 1998, he was Manager of the National Program for Information and Communications Technologies at the Plan Nacional de I+D, National Research and Development Plan of the Spanish Ministry of Education and Science, Madrid, Spain. He is Project Manager for the BEMs at 30 and 44 GHz for the radiometers of the PLANCK mission. His main areas of activities and contributions have been microwave circuits and systems, including MMICs from RF (a few megahertz) up to 50 GHz. His current research interests are low-noise millimeter-wave amplifiers and low-noise millimeter-wave receivers.

Luisa la de Fuente (S'92–M'98) was born in Reinosa, Spain, in 1968. She graduated from the Universidad de Cantabria, Santander, Spain, in 1991 and received the Doctoral degree in electronics engineering from the Universidad de Cantabria, in 1997.

From 1992 to 1993, she was an Associate Teacher with the Department of Electronics, Universidad de Cantabria. She is currently a Professor with the Departamento de Ingeniería de Comunicaciones, Universidad de Cantabria. Her main research interests include design and testing of microwave circuits in both hybrid and monolithic technologies, in particular, the design of low-noise amplifiers and microwave mixers.

Juan Pablo Pascual (S'92–M'97) was born in Santander, Spain, in 1968. He received the M. degree in electronics (with honors) and Ph.D. degree in electronic engineering from the Universidad de Cantabria, Santander, Spain, in 1990 and 1996, respectively.

He is currently with the Departamento de Ingeniería de Comunicaciones, Universidad de Cantabria, Escuela Técnica Superior de Ingenieros de Telecomunicación (ETSI), Universidad de Cantabria. His research interests are high electron-mobility transistor (HEMT) and HBT modeling, MMIC design methodology of linear and nonlinear functions, and system simulation. He has been involved in modeling and design projects with industries from Spain and with international companies and institutions like Daimler Chrysler, the Technical University of Darmstadt (where he stayed during 1999), and the PLANCK scientific mission consortium.

Angel Mediavilla was born in Santander, Spain, in 1955. He graduated in 1978 and received the Doctor of Physics (electronic) degree (with honors) from the Universidad de Cantabria, Santander, Spain, in 1983.

From 1980 to 1983, he was Ingenieur Stagiere with THOMSON-CSF, Orsay, France. He is currently a Professor with the Departamento de Ingeniería de Comunicaciones, Universidad de Cantabria. He possesses a wide experience in the analysis and optimization of nonlinear microwave active devices in both hybrid and monolithic technologies. He is currently involved in the area of nonlinear MESFET/HEMT and HBT device modeling with special application to the large-signal computer design and intermodulation properties.

Neil Roddis is Leader of the Receivers Engineering Group, Jodrell Bank Observatory, a part of the School of Physics and Astronomy, The University of Manchester, Cheshire, U.K. He is involved in all RF aspects of the radio astronomy instrumentation at the Jodrell Bank Observatory. As well as the PLANCK LFI, this includes the current upgrade to the MERLIN/VLBI National Facility, and the European PHAROS project to develop cryogenic low-noise phased arrays. His current areas of interest include low-noise measurement systems, high-temperature superconductors applications to radio astronomy, and broad-band feed design.

Danielle Kettle is currently working toward the Ph.D. degree in electronic and electrical engineering at The University of Manchester, Cheshire, U.K.

She is a Microwave Engineer with the Jodrell Bank Observatory, a part of the School of Physics and Astronomy, The University of Manchester. She has developed the acquisition system to demonstrate the PLANCK LFI differential radiometer concept using the first 30-GHz receiver prototypes. She has designed and tested several MMICs used in radio-astronomy projects such as the European Union (EU) funded FARADAY project. She has collaborated in the testing and development of FEMs at 30 and 44 GHz of the differential radiometers in the European Scientific mission PLANCK. Her current interest is the measurement of HEMT devices made at both ambient and cryogenic temperatures with a goal to develop small-signal models and noise models. Her research includes the characterization and application of state-of-the-art discrete InP and GaAs HEMT devices to very low-noise radio-astronomy receivers.

W. Frank Winder was born in Farnworth, U.K., on August 20, 1941. He received the B.Eng. and Ph.D. degrees in electrical and electronic engineering from Sheffield University, Sheffield, U.K., in 1962 and 1965 respectively.

From 1965 to 1994, he was with Ferranti International, where he was initially involved with low-noise parametric amplifiers and then with microwave subsystem design. He was then involved with the design of radar towed targets for use with the U.K. Royal Navy and Royal Air Force. From 1994 to 1998, he continued his work with Matra Marconi Space and subsequently undertook consultancy work in this field. He accepted a post in 1999 as a Senior Design Engineer with the Jodrell Bank Observatory, a part of the School of Physics and Astronomy, The University of Manchester, Cheshire, U.K., where he is involved with the development of 30- and 44-GHz low-noise amplifiers for the PLANCK Surveyor project using InP HEMT technology. He is also responsible for the design integration of these amplifiers and associated components into the cryogenically cooled radiometer FEMs. His current interests are the design of low-noise amplifiers and other millimeter-wave components for radio-astronomy applications.

Lluis Pradell i Cara was born in Barcelona, Catalunya, Spain, in 1956. He received the Telecommunication Engineering degree and Dr. degree in telecommunication engineering from the Universitat Politècnica de Catalunya (UPC), Barcelona, Spain, in 1981 and 1989, respectively.

From 1981 to 1985, he was with Mier-Allende, Barcelona, Spain, as an RF and Microwave System Design Engineer. In 1985, he joined the faculty at UPC, where he became Associate Professor in 1990. Since 1985, he has taught courses on microwave circuits and performed research on models for microwave active devices (MESFETs, HEMTs, HBTs), multimodal models for guiding structures and transitions [microstrips, finlines, slotlines, coplanar waveguides (CPWs)], on-wafer measurement techniques (network-analyzer calibration, noise parameters), development of microwave and millimeter-wave circuits (equipment for space applications, point-to-multipoint broad-band equipment, RF microelectromechanical systems (MEMS) devices), in the frequency range of 1–75 GHz.

Pedro de Paco was born in Badalona, Spain, in 1972. He received the Telecommunication Engineering degree and Ph.D. degree from the Escola Técnica Superior d'Enginyeria (ETSE) de Telecomunicació, Universitat Politécnica de Catalunya (UPC), Barcelona, Spain, in 1997 and 2003, respectively.

In 1998, he joined the Electromagnetic and Photonic Engineering Group (EEF), UPC, as a graduate student. Since June 2004, he has been with the Universidad Autonoma de Barcelona, Barcelona, Spain, where he teaches courses on microwave circuits and systems. His research interests are in the area of microwave and millimeter-wave circuits and systems design and device modeling.